Investigation of germanium Raman lasers for the mid infrared

Investigation of germanium Raman lasers for the mid-infrared

Francesco De Leonardis,[1] Benedetto Troia,[1] Richard A. Soref,[2] and Vittorio M. N. Passaro[1,*]

[1]*Photonics Research Group, Dipartimento di Ingegneria Elettrica e dell'Informazione, Politecnico di Bari, Via Edoardo Orabona n. 4, 70125 Bari, Italy*

[2]*Department of Physics and the Engineering Program, The University of Massachusetts, Boston, Massachusetts 02125, USA*

[*]*vittorio.passaro@poliba.it*

Abstract: In this paper we present a detailed theoretical investigation of integrated racetrack Raman lasers based on the germanium material system operating in the mid-infrared beyond the germanium two-photon absorption cut-off wavelength of 3.17 μm. The effective Raman gain has been estimated in waveguides based on germanium-on-silicon, germanium-on-SOI and germanium-on-Si3N4 technology platforms as a function of their crystallographic orientations. Furthermore, general design guidelines have been determined by means of a comparative analysis of Raman laser performance, i.e. the threshold power, polarization and directionality of the excited Stokes signals as a function of racetrack cavity length and directional-coupler dimensions. Finally, the emitted Raman laser power has been evaluated as a function of overall propagation losses and operative wavelengths up to 3.8 μm, while the time dynamics of Raman lasers has been simulated assuming continuous and pulse waves as input pump signals.

OCIS codes: (190.5890) Scattering, stimulated; (130.3060) Infrared; (130.4310) Nonlinear.

References and links

1. R. A. Soref, "The past, present, and future of silicon photonics," IEEE J. Sel. Top. Quantum Electron. **12**(6), 1678–1687 (2006).
2. R. A. Soref, "Mid-infrared photonics in silicon and germanium," Nat. Photonics **4**(8), 495–497 (2010).
3. B. Jalali, "Nonlinear optics in the mid-infrared," Nat. Photonics **4**(8), 506–508 (2010).
4. T. Baehr-Jones, A. Spott, R. Ilic, A. Spott, B. Penkov, W. Asher, and M. Hochberg, "Silicon-on-sapphire integrated waveguides for the mid-infrared," Opt. Express **18**(12), 12127–12135 (2010).
5. F. De Leonardis, B. Troia, and V. M. N. Passaro, "Mid-IR optical and nonlinear properties of germanium on silicon optical waveguides," J. Lightwave Technol. **32**(22), 3747–3757 (2014).
6. N. K. Hon, R. Soref, and B. Jalali, "The third-order nonlinear optical coefficients of Si, Ge, and $Si_{1-x}Ge_x$ in the midwave and longwave infrared," J. Appl. Phys. **110**(1), 011301 (2011).
7. G. Roelkens, U. Dave, A. Gassenq, N. Hattasan, C. Hu, B. Kuyken, F. Leo, A. Malik, M. Muneeb, E. Ryckeboer, D. Sanchez, S. Uvin, R. Wang, Z. Hens, R. Baets, Y. Shimura, F. Gencarelli, B. Vincent, R. Loo, J. Van Campenhout, L. Cerutti, J. B. Rodriguez, E. Tournie, X. Chen, M. Nedeljkovic, G. Mashanovich, L. Shen, N. Healy, A. C. Peacock, X. Liu, R. Osgood, and W. Green, "Silicon-based photonic integration beyond the telecommunication wavelength range," IEEE J. Sel. Top. Quantum Electron. **20**(4), 394–404 (2014).
8. G. Z. Mashanovich, F. Y. Gardes, D. J. Thomson, Y. Hu, K. Li, M. Nedeljkovic, J. Soler Penades, A. Z. Khokhar, C. J. Mitchell, S. Stankovic, R. Topley, S. A. Reynolds, Y. Wang, B. Troia, V. M. N. Passaro, C. G. Littlejohns, T. Dominguez Bucio, P. R. Wilson, and G. T. Reed, "Silicon photonic waveguides and devices for near- and mid-IR applications," IEEE J. Sel. Top. Quantum Electron. **21**(4), 8200112 (2015).
9. R. A. Soref, S. J. Emelett, and W. R. Buchwald, "Silicon waveguided components for the long-wave infrared region," J. Opt. A **8**(10), 840–848 (2006).
10. Y. C. Chang, V. Paeder, L. Hvozdara, J. M. Hartmann, and H. P. Herzig, "Low-loss germanium strip waveguides on silicon for the mid-infrared," Opt. Lett. **37**(14), 2883–2885 (2012).
11. A. Malik, M. Muneeb, Y. Shimura, J. Van Campenhout, R. Loo, and G. Roelkens, "Germanium on silicon planar concave grating wavelength (de)multiplexers in the mid infrared," Appl. Phys. Lett. **103**(16), 161119 (2013).

#239685 Received 23 Apr 2015; revised 5 Jun 2015; accepted 8 Jun 2015; published 23 Jun 2015

12. A. Malik, M. Muneeb, S. Pathak, Y. Shimura, J. Van Campenhout, R. Loo, and G. Roelkens, "Germanium on silicon mid infrared arrayed waveguide grating multiplexers," IEEE Photon. Technol. Lett. **25**(18), 1805–1808 (2013).
13. R. A. Soref, "Mid infrared 2 × 2 electro optical switching by silicon and germanium three waveguide and four waveguide directional couplers using free carrier injection," Photon. Res. **2**(5), 102–110 (2014).
14. A. Malik, S. Dwivedi, L. Van Landschoot, M. Muneeb, Y. Shimura, G. Lepage, J. Van Campenhout, W. Vanherle, T. Van Opstal, R. Loo, and G. Roelkens, "Ge-on-Si and Ge-on-SOI thermo-optic phase shifters for the mid-infrared," Opt. Express **22**(23), 28479–28488 (2014).
15. L. Shen, N. Healy, C. J. Mitchell, J. S. Penades, M. Nedeljkovic, G. Z. Mashanovich, and A. C. Peacock, "Mid-infrared all-optical modulation in low-loss germanium-on-silicon waveguides," Opt. Lett. **40**(2), 268–271 (2015).
16. M. Nedeljkovic, J. Soler Penadés, C. J. Mitchell, A. Z. Khokhar, S. Stanković, T. Dominguez Bucio, C. G. Littlejohns, F. Y. Gardes, and G. Z. Mashanovich, "Surface grating coupled low loss Ge-on-Si rib waveguides and multimode interferometers," IEEE Photon. Technol. Lett. **27**(10), 1040–1043 (2015).
17. L. Shen, N. Healy, C. J. Mitchell, J. Soler Penades, M. Nedeljkovic, G. Z. Mashanovich, and A. C. Peacock, "Two-photon absorption and all-optical modulation in germanium-on-silicon waveguides for the mid-infrared," Opt. Lett. **40**(10), 2213–2216 (2015).
18. L. Carletti, P. Ma, Y. Yu, B. Luther-Davies, D. Hudson, C. Monat, R. Orobtchouk, S. Madden, D. J. Moss, M. Brun, S. Ortiz, P. Labeye, S. Nicoletti, and C. Grillet, "Nonlinear optical response of low loss silicon germanium waveguides in the mid-infrared," Opt. Express **23**(7), 8261–8271 (2015).
19. C. Wolff, R. Soref, C. G. Poulton, and B. J. Eggleton, "Germanium as a material for stimulated Brillouin scattering in the mid-infrared," Opt. Express **22**(25), 30735–30747 (2014).
20. H. Rong, S. Xu, O. Cohen, O. Raday, M. Lee, V. Sih, and M. Paniccia, "A cascaded silicon Raman laser," Nat. Photonics **2**(3), 170–174 (2008).
21. F. De Leonardis, B. Troia, and V. M. N. Passaro, "Design rules for Raman lasers based on SOI racetrack resonators," IEEE Photon. Journal **6**(5), 6648677 (2013).
22. V. M. N. Passaro and F. De Leonardis, "Investigation of SOI Raman lasers for mid-infrared gas sensing," Sensors (Basel) **9**(10), 7814–7836 (2009).
23. J.-H. Fournier-Lupien, S. Mukherjee, S. Wirths, E. Pippel, N. Hayazawa, G. Mussler, J. M. Hartmann, P. Desjardins, D. Buca, and O. Moutanabbir, "Strain and composition effects on Raman vibrational modes of silicon-germanium-tin ternary alloys," Appl. Phys. Lett. **103**(26), 263103 (2013).
24. F. Cerdeira, C. J. Buchenauer, F. H. Pollak, and M. Cardona, "Stress-induced Shift of First-Order Raman Frequencies of Diamond and Zinc-Blende-Type Semiconductor," Phys. Rev. B **5**(2), 580–593 (1972).
25. Comsol Multiphysics by COMSOL©, single license (2005).
26. F. De Leonardis, B. Troia, C. E. Campanella, and V. M. N. Passaro, "Thermal and stress influence on performance of SOI racetrack resonator Raman lasers," J. Opt. **16**(8), 085501 (2014).

1. Introduction

Germanium (Ge) has been seen for more than a decade as a very promising material for extending the operation of integrated photonic circuits from the conventional near-infrared (NIR) wavelength range to the vibrant mid-infrared (MIR) spectral window [1,2]. Some of the most intriguing applications achievable by this material are the use of a Ge-based photonic chip for ultra-high performance sensing in the 8 to 14 μm wavelength range where several chemical and biochemical species exhibit very strong fingerprints, as well as the excitation of nonlinearities in the MIR [3]. Indeed, Ge is characterized by a very wide transparency extending out to 16 μm, where the conventional silicon-on-insulator (SOI) technology platform cannot be used because of the extremely high absorption loss of silicon dioxide (SiO_2) beyond 4 μm [4]. On the other hand, we have already demonstrated in a previous work [5] how different Ge-based technology platforms, such as Ge-on-Si (GOS), exhibit much lower loss than SOI technology in the MIR. Furthermore, the absence of the nonlinear losses such as two-photon-absorption (TPA) as well as the TPA-induced free-carrier-absorption (FCA) effect beyond the cut-off wavelength of 3.17 μm, allows nonlinearities to be excited very efficiently since detrimental band-to-band transitions are inhibited [6].

Recently, huge research efforts have been carried out in order to experimentally demonstrate fundamental photonic devices based on Ge technology (e.g., germanium-on-silicon (GOS) and germanium-on-SOI) and operating in the MIR [7,8]. For example, low-loss monocrystalline GOS waveguides have been proposed [9] and experimentally demonstrated for the first time at the wavelength of 5.8 μm [10], having propagation losses of 3.6 ± 0.8 dB/cm and bend losses of 0.12 dB for a 90° bend with a radius of 115 μm. Moreover, DEMUX based on planar concave gratings [11] as well as MUX based on arrayed waveguide

#239685 Received 23 Apr 2015; revised 5 Jun 2015; accepted 8 Jun 2015; published 23 Jun 2015

gratings [12] have been demonstrated in a GOS platform in the wavelength range of 5.0-5.4 μm. Furthermore, the design of a 2 × 2 electro-optical switch based on Si and Ge channel waveguides operating in the wavelength range of 1.3-12 μm has been reported [13]. Very recently, GOS and GOI thermo-optic phase shifters have been fabricated and characterized for the first time at 5 μm [14]. Moreover, MIR all-optical modulation has been achieved in GOS waveguides [15] and record low losses of 0.6 dB/cm have been measured in GOS rib waveguides [16], both at the MIR wavelength of 3.8 μm.

A few studies on nonlinearities in Ge-based photonic waveguides and devices operating in the MIR wavelength range have also been reported [17]. Actually, the nonlinear optical response of low loss $Si_{0.6}Ge_{0.4}$/Si waveguides in the MIR wavelength range of 3.25-4.75 μm by means of picosecond optical pulses have been investigated with the experimental estimation of the Kerr nonlinear refractive index [18]. Furthermore, nonlinear optical properties such as the stimulated Brillouin scattering (SBS) [19] and the stimulated Raman scattering (SRS) [5], have been theoretically investigated in GOS waveguides [5] and in the new Germanium-on-Silicon-Nitride (GON) waveguide technology platform [19], revealing competitive advantages with respect to the operation of Si- and Ge-based devices in the NIR wavelength range.

In this paper we present, for the first time to the best of our knowledge, a theoretical and comparative investigation of SRS in racetrack resonators based on Ge-based material systems, i.e., GOS, GOI and GON. Actually, the Raman effect has been widely used in the NIR for achieving efficient laser emission around 1.55 μm in SOI-based photonic devices [20,21]. However, apart from a theoretical simulation of SOI Raman lasing for sensing purposes in the MIR [22], Raman effect devices based on Ge technology platforms have not been investigated yet. Consequently, fundamental equations and theoretical assumptions are presented here in Section 2 for the modelling and simulation of nonlinearities in Ge-based racetrack resonators. Then, general design guidelines of Ge-based Raman lasers operating in the MIR wavelength range of 3.2-3.8 μm are reported in Section 3. In particular, a detailed investigation of the theoretical performance such as the lasing threshold, the laser efficiency as well as the polarization and directionality of co- and counter-propagating Stokes signals inside the racetrack cavity, is presented as a function of geometrical and optical parameters, e.g., the cavity length and power coupling factors of the directional couplers. Finally, Section 4 summarizes the conclusions.

2. Theoretical background

In the analysis proposed in this paper, racetrack resonators are investigated for the design and simulation of integrated Raman lasers. Actually, racetrack microcavities are usually preferred to standard rings since long roundtrips can be achieved in relatively small footprints. In fact, this represents an advantage because the overall Raman gain can be improved by designing long cavities, even of the order of few mm where the only limitation is practically imposed by propagation losses [21]. With reference to Fig. 1(a), the input optical pump, $P_{in} = |S_p|^2$, which propagates into the input bus waveguide, is then coupled to the racetrack resonator by means of a directional coupler (DC) characterized by a gap, g, and a length, L_{coup}. Moreover, an additional bus waveguide with a symmetric DC has been considered at the bottom of the device in order to investigate the laser operation when counter-propagating waves are also generated into the microcavity. As a result, by considering the input port as sketched in Fig. 1(a), the top bus waveguide allows the readout of co-propagating signals (i.e., blue and violet arrows), while the bus waveguide at the bottom allows the detection of counter-propagating signals (i.e., red and orange arrows), which propagate counter-clockwise.

Three different Si-based technology platforms have been examined in this investigation of innovative Raman lasers based on Germanium waveguides and operating in the mid-IR wavelength range: GOS, GOI, and GON. As an example, fully-etched waveguide cross-

#239685 Received 23 Apr 2015; revised 5 Jun 2015; accepted 8 Jun 2015; published 23 Jun 2015

sections with a width, W, and an height, H, are sketched in Fig. 1(b) in case of the GOS technology platform and in Fig. 1(c) in the case of the other two material systems where an upper silicon layer with a thickness of 100 nm is assumed over the low refractive index layer (i.e., SiO_2 or Si_3N_4). In Fig. 1(d), z represents the propagation direction of the bus waveguides and the angle θ represents a possible orientation of the z crystallographic axis of the single-crystal Ge core with respect to z, with x-z in the x-z plane.

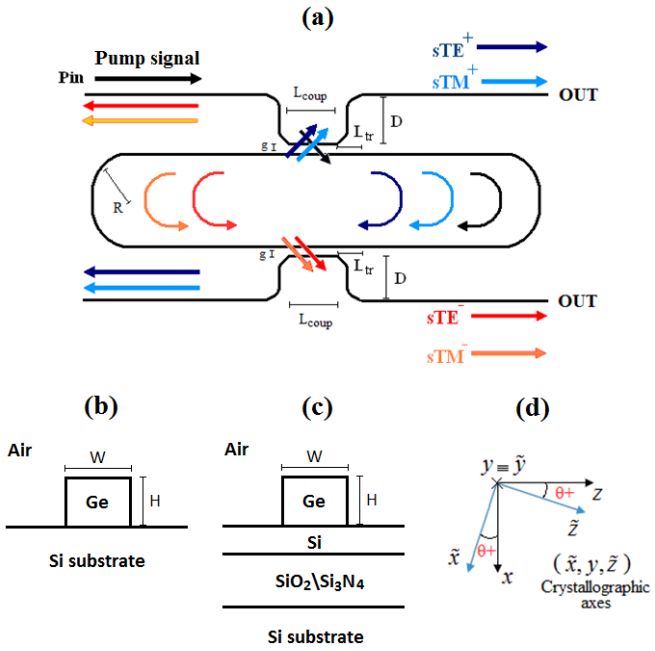

Fig. 1. (a) Schematic architecture of a Raman laser based on a racetrack resonator coupled to the external bus waveguides. Waveguide cross-sections based on (b) GOS and (c) GOI/GON technology platforms with (d) the crystallographic axes.

The input pump wave, previously indicated as S_p, can be aligned with the quasi-TE (i.e., transverse electric) or quasi-TM (i.e., transverse magnetic) polarization, thus inducing Stokes waves aligned with quasi-TE or quasi-TM modes, depending on the specific laser operation. Finally, input and output buses, DCs, as well as the racetrack resonator are always assumed to be based on the same waveguide structure (e.g., rib, wire, to name a few).

A self-consistent model already proposed by us in [21] and based on a full vectorial approach has been used for the modelling and simulation of Raman lasers. The model is based on a set of partial differential equations for the nonlinear coupling between pump (p) and fundamental Stokes (s) waves, which propagate along the microcavity. In particular, for each state of polarization (i.e., quasi-TE, or quasi-TM) two Stokes waves have been considered: a co-propagating or a counter-propagating wave with respect to propagation direction of the pump signal. It is worth noting that the flexibility and generality of the model, which has already been applied for the investigation of SOI Raman lasers working in the NIR, allows us to extend its application to novel platforms such as the GOS, GOI and GON, where the TPA and FCA effects can be neglected. Indeed, the detrimental effects induced by TPA and FCA can be avoided if nonlinear Ge-based devices are operated at MIR wavelengths longer than the TPA cut-off wavelength, equal to $\lambda_{Ge}^{TPA} = 3.17$ μm [6]. Furthermore, the model takes into account all the nonlinear effects involved in such integrated devices, i.e. SRS, Self-Phase-Modulation (SPM) and Cross-Phase-Modulation (XPM) effects induced by the Kerr nonlinearity, polarization effect, emission directionality of the Stokes waves, mismatch between the input beam wavelengths and the microcavity resonance wavelengths as well as

#239685 Received 23 Apr 2015; revised 5 Jun 2015; accepted 8 Jun 2015; published 23 Jun 2015

the coupling mechanism between the microcavity and input/output bus waveguides. Then, the differential equation system can be solved after evaluating a number of optical parameters. To give an example, the overall photon decay time τ_i of the pump and Stokes wave inside the cavity can be considered as a function of three parameters, i.e. linear loss (τ_i^l), input bus coupling ($\tau_i^{c,1}$) and output bus coupling ($\tau_i^{c,2}$), where *i* is the index that indicates alternatively the pump (*p*) or the Stokes (*s*) wave (i.e., *i* = *p*, *s*). In particular, the decay time due to losses can also be calculated as a function of the overall linear loss coefficient (α_{loss}) by means of the relationship $\tau_i^l = 1/(\alpha_{loss,i} v_{g,i})$, with $v_{g,i}$ the group velocity. In addition, the coupling time constants $\tau_i^{c,m}$ (*m* = 1, 2) depend on the coupling factor $\kappa_{i,m}^2$ (i.e., the power fraction of the input pump or Stokes wave coupled from the racetrack resonator to the external bus waveguides and *vice versa*), by means of Eq. (1):

$$\tau_i^{c,m} = L_{cavity} \Big/ \left(\kappa_{i,m}^2 v_{g,s} \right) \tag{1}$$

where L_{cavity} is the physical circumferential cavity length.

With reference to the fully-etched Ge waveguide sketched in Figs. 1(b) and 1(c) (let us name it as *wire waveguide*), the total loss coefficient can be calculated by means of Eq. (2), for each of the technology platforms assumed in this investigation [5]:

$$\alpha_{loss} = \sum_d \Gamma_d \alpha_d \tag{2}$$

Actually, α_d is the propagation loss coefficient valuated in the *d*-th subdomain, i.e. the Ge wire waveguide, the Si slab layer in the GOI and GON technology platforms, and the Si bulk. Similarly, Γ_d, is the field confinement factor in the *d*-th subdomain as above, which can be calculated according to Eq. (3) [5]:

$$\Gamma_d = \frac{n_d c_0 \varepsilon_0 \iint_d |\mathbf{e}_i|^2 \, dxdy}{\iint \mathrm{Re}\{\mathbf{e}_i \times \mathbf{h}_i^*\} \cdot \hat{\mathbf{e}}_z \, dxdy} \tag{3}$$

where n_d is the refractive index of the *d*-th subdomain and $\hat{e}_z$ is the unit vector along the *z* propagation direction. In Eq. (3) as well as in the following equations, $\boldsymbol{e}_p$, $\boldsymbol{e}_{s+}$ and $\boldsymbol{e}_{s-}$ are the electric field vectors of the pump (*p*) and Stokes (*s*) modes, respectively, with real transverse and imaginary longitudinal components. In particular, $\boldsymbol{e}_{s+}$ represents the Stokes wave co-propagating with the pump inside the resonator, while $\boldsymbol{e}_{s-}$ indicates the counter-propagating Stokes mode, which, by definition, has the same transverse components as $\boldsymbol{e}_{s+}$ but with the longitudinal component equal to the complex conjugate.

With the aim of presenting a comparative investigation on the SRS effect induced in racetrack resonators based on GOS, GOI and GON technology platforms and operating in the vibrant MIR wavelength range, it is also crucial to analyse the directionality of the emitted Stokes waves with respect to the input pump beam as well as the specific combinations between the states of pump/Stokes polarization, so that the best operative conditions for an efficient lasing effect can be found. In this context, a very useful parameter is the effective Raman gain $g_{s,\rho}^{\sigma}$ of the Stokes wave propagating in the racetrack and characterized by a polarization state and a propagation direction with respect to the pump, indicated by the indices σ (TE, TM) and ρ (+ , -), respectively. This parameter $g_{s,\rho}^{\sigma}$ is defined as [21]:

$$g_{s,\rho}^{\sigma}(\theta) = g_{bulk,Ge}^{SRS} \Big/ A_{s\rho\sigma,p}^{SRS} \tag{4}$$

#239685 Received 23 Apr 2015; revised 5 Jun 2015; accepted 8 Jun 2015; published 23 Jun 2015

In Eq. (4), $g_{bulk,Ge}^{SRS}$ is the Raman gain of the bulk Ge material and $A_{s\rho\sigma,p}^{SRS}$ is the SRS effective modal area defined in Eq. (5), assuming the pump signal with a fixed polarization (TE or TM) and the Stokes wave polarization state depending on the physics of the device (e.g., waveguide dimensions, power coupling coefficients and nonlinear effective areas):

$$A_{s\rho\sigma,p}^{SRS}=\frac{4\mu_0\left(\hat{N}_{s\sigma}\hat{N}_p\right)}{\varepsilon_0 n_s n_p}\left\{\iint\left[\begin{array}{l}\left|\mathbf{e}_{s\rho\sigma}\right|^2\left|\mathbf{e}_p\right|^2+\left|\mathbf{e}_{s\rho\sigma}\cdot\mathbf{e}_p\right|^2\\-2\left(\left|\tilde{e}_{s\rho\sigma}^x\right|^2\left|\tilde{e}_p^x\right|^2+\left|\tilde{e}_{s\rho\sigma}^y\right|^2\left|\tilde{e}_p^y\right|^2+\left|\tilde{e}_{s\rho\sigma}^z\right|^2\left|\tilde{e}_p^z\right|^2\right)\end{array}\right]dxdy\right\}^{-1} \quad (5)$$

The normalization coefficients $\hat{N}_{s\sigma}$ and $\hat{N}_p$ are defined in [21], while the terms n_p and n_s are the Ge refractive indices at the pump and Stokes wavelengths, respectively, calculated by means of Sellmeier's equations [5]. The effective Raman gain is also influenced by the Ge waveguide-core orientation since the electro-magnetic field is assumed to be evaluated in the waveguide coordinate system (*x,y,z*), generally rotated by an angle θ with respect to the Ge crystallographic axes ($\tilde{x},\tilde{y},\tilde{z}$), as sketched in Fig. 1(d).

Finally, the effective modal areas that include the SPM and XPM effects as induced by Kerr nonlinearity have been calculated according to Eq. (6):

$$A_{i,j}^{Kerr}=\frac{4\mu_0\left(\hat{N}_i\hat{N}_j\right)}{\varepsilon_0 n_i n_j}\left\{\iint\left[\begin{array}{l}\frac{\varsigma}{3}\left(\left|\mathbf{e}_i\right|^2\left|\mathbf{e}_j\right|^2+\left|\mathbf{e}_i\cdot\left(\mathbf{e}_j\right)^*\right|^2+\left|\mathbf{e}_i\cdot\mathbf{e}_j\right|^2\right)\\+(1-\varsigma)\left(\left|\tilde{e}_i^x\right|^2\left|\tilde{e}_j^x\right|^2+\left|\tilde{e}_i^y\right|^2\left|\tilde{e}_j^y\right|^2+\left|\tilde{e}_i^z\right|^2\left|\tilde{e}_j^z\right|^2\right)\end{array}\right]dxdy\right\}^{-1} \quad (6)$$

$$i=p,s_{+TE},s_{-TE},s_{+TM},s_{-TM};\ j=p,s_{+TE},s_{-TE},s_{+TM},s_{-TM}$$

where ς is the anisotropy factor for the Kerr effect [6]. In conclusion, it is worth specifying that the nonlinear Kerr refractive index $n_2(\omega)$ has been evaluated by using the equation derived via the Kramers-Kronig relation [6].

3. Numerical results

In this Section, a detailed investigation of integrated Raman lasers assumed to operate in the wavelength range of 3.2-3.8 μm and based on Ge waveguides in GOS, GOI and GON technology platforms, is reported.

The calculation of the angular frequency of the phonons involved in the SRS process represents a preliminary step toward the overall model execution. To this purpose, some authors have recently demonstrated that the experimental Raman shift in bulk Ge matches the following relationship with a very good agreement [23]:

$$\Omega_{Ge}=\Omega_{Ge}^0+b\varepsilon \quad (7)$$

where Ω_{Ge}^0 = 301 cm^{-1} corresponds to the Raman shift in bulk Ge without any strain ε, and the term b = –415 cm^{-1} [23,24] is the linear coefficient associated with the strain.

Actually, a strain can be induced in the Ge bulk material following a deposition process over different material layers (e.g., Si). Indeed, after annealing at high temperature, the mismatch in thermal expansivity between Ge and Si layers will result in thermally induced stresses at the operating temperature (typically room temperature, 27 °C). Consequently, the difference $\Omega_{Ge}-\Omega_{Ge}^0$ can be calculated by numerically solving (i.e., by FEM [25]) the stress field in the waveguide as a function of the annealing temperature. Then, the static equilibrium equation is solved, thus simultaneously satisfying the thermal effects, the stress–strain and the strain-displacement relationships for the displacement variables along *x*, *y*, and *z* directions, as well as the proper boundary conditions. Further details of this approach are reported in [26].

#239685 Received 23 Apr 2015; revised 5 Jun 2015; accepted 8 Jun 2015; published 23 Jun 2015

Finally, once the average strain distribution into the Ge waveguide has been calculated, the application of Eq. (7) gives the plot in Fig. 2.

The parameters listed in Table 1 have been used to perform strain simulations. In particular, $E_{Y,M}$ is the Young's modulus of the material M, ν_M is the Poisson'ratio of the material M and $\alpha_{thermal,M}$ is the thermal expansion coefficient of the material M as well.

Table 1. Physical parameters used in the simulations.

Parameters	Values
$E_{Y,Ge}$	103(GPa)
$E_{Y,Si}$	130 (GPa)
$E_{Y,SiO2}$	76.7 (GPa)
$E_{Y,Si3N4}$	160(GPa)
ν_{Ge}	0.26
ν_{Si}	0.19
ν_{SiO2}	0.42
ν_{Si3N4}	0.253
$\alpha_{thermal,Ge}$ at 293 K	5.95×10^{-6} (K^{-1})
$\alpha_{thermal,Si}$ at 293 K	2.5×10^{-6} (K^{-1})
$\alpha_{thermal,SiO2}$ at 293 K	3.5×10^{-7} (K^{-1})
$\alpha_{thermal,Si3N4}$ at 293 K	3.75×10^{-6} (K^{-1})

A computation spatial domain of about 60 μm^2 with 90,000 mesh triangular elements has been used for an accurate stress calculation, while a much smaller computational domain has been taken into account in electromagnetic simulations. In particular, large domains are preferred in stress analysis since the overall wafer height and width must be large enough to neglect the influence of boundary effects on the calculated stresses in thin films and waveguides. Finally, as the Ge layer is always deposited on Si in all the Ge technology platforms aforementioned, simulation results indicate very small differences between GOS, GOI, and GON cross sections. Consequently, only the Raman shift calculated in the GOS platform is plotted in Fig. 2 as a function of the annealing temperature varied in the range of 300-1000 °C.

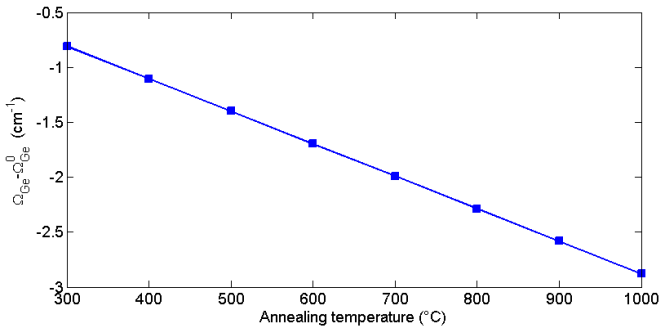

Fig. 2. Germanium Raman shift as a function of the annealing temperature.

The investigation of the SRS effect in Ge waveguides consists also in the specific evaluation of the effective Raman gain to be performed according to Eqs. (4) and (5). It is worth noting that, unlike the conventional Si-based material systems, an experimental Raman gain coefficient of Ge has not been reported yet in the MIR. However, as detailed in [6], $g^{SRS}_{bulk,Ge}$ can be estimated by using the well-known Si experimental effective Raman gain values, with the result that, for a given Stokes angular frequency, $g^{SRS}_{bulk,Ge}$ is 4.5 times larger than $g^{SRS}_{bulk,Si}$. Under this assumption, the effective Raman-gain (i.e., $g^{\sigma}_{s\rho}$) is plotted in Figs. 3(a) and 3(b) as a function of the waveguide orientation θ, ranging from 0° ([001]) to 45° ([011]), for co-

#239685 Received 23 Apr 2015; revised 5 Jun 2015; accepted 8 Jun 2015; published 23 Jun 2015

propagating and counter-propagating fundamental Stokes waves with respect to the pump beam and for mixed and fixed polarization, respectively.

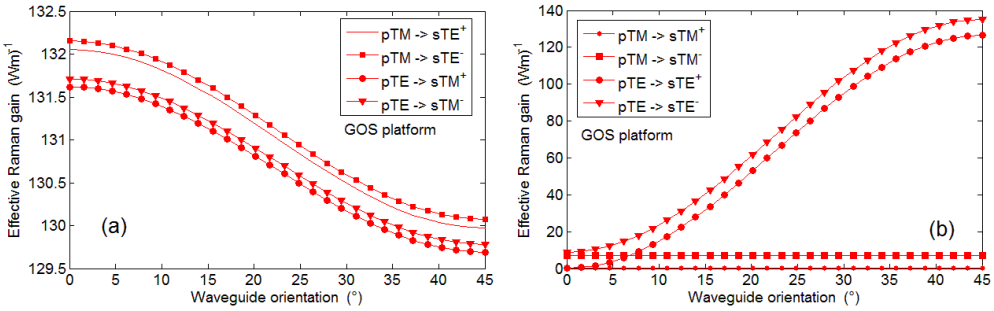

Fig. 3. Effective Raman gain versus the waveguide orientation θ for co-propagating and counter-propagating pump and Stokes waves; (a) mixed polarization, (b) fixed polarization.

With reference to Figs. 1(b) and 1(c) a wire Ge waveguide with dimensions W = 2 μm, H = 2 μm, designed at the MIR operating wavelength λ_p = 3.2 μm μm (a CW OPO source with P_{max} = 5 W can be used in experiments) has been taken into account in simulations, thus resulting in the Stokes wavelength λ_s = 3.539 μm. However, it is worth specifying that the same analysis can be performed in the case of Ge-based rib waveguides, but simulation results have revealed that the effective modal areas increase exponentially as a function of shallower etch depth, thus confirming fully-etched waveguides as the most suitable for achieving very high Raman effective gains. A custom-made algorithmic procedure based on full-vectorial finite-element method (FEM Electromagnetic module [25]) has been implemented for the calculation of the effective modal areas. As a result, some considerations can be outlined as follows: the excitation $p_{TM} \rightarrow s_{TM}^{\rho}$ (ρ = + , –) does not occur due to the very weak effective gain, as shown in Fig. 3(b), while the other combinations can exhibit $g_{s\rho}^{\sigma}$ up to roughly 132 (Wm)$^{-1}$. Moreover, the comparative analysis of Figs. 3(a) and 3(b) reveals two opposite trends of the effective Raman gains as a function of the angle θ, in the case of mixed or fixed polarizations. In fact, $g_{s\rho}^{\sigma}$ decreseas from θ = 0° to θ = 45° with mixed polarizations, while it increases in the case of constant polarizations. In addition, the effective Raman gain varies in the range [129.5-132.5] (Wm)$^{-1}$ in the case of mixed polarizations, confirming that the Stokes emission could be allowed for both typical waveguide orientations. On the contrary, $g_{s\rho}^{\sigma}$ varies in the very wide range [0-140] (Wm)$^{-1}$ in the case of fixed polarizations, thereby allowing the Raman emission at 45° while totally inhibiting it at 0°. In conclusion, Fig. 3 demonstrates that the counter-propagating Stokes emission is always preferred with respect to the co-propagating Stokes wave, independent of the pump polarization state.

Actually, although the plot in Fig. 3 refers only to the GOS technology platform, simulations in case of GOI and GON platforms have given very similar results because of the large confinement of the optical mode in the Ge wire waveguide. Some reprentative simulation results are summarized in Table 2, suggesting the excitations $p_{TE} \rightarrow s_{TE}^{-}$, $p_{TE} \rightarrow s_{TM}^{-}$ and $p_{TM} \rightarrow s_{TE}^{-}$, as the operative conditions with the highest effective Raman gain. Following the previous analysis, a parametric investigation of the threshold powers required for the excitation of the Raman lasing effect in racetrack resonators as a function of the DC power coupling factors for the pump and Stokes waves, indicated as κ_p^2 and κ_s^2, respectively, has been carried out.

#239685 Received 23 Apr 2015; revised 5 Jun 2015; accepted 8 Jun 2015; published 23 Jun 2015

Table 2. Effective Raman gain.

Platform	Effective Raman gain $(Wm)^{-1}$					
	pTE→sTE⁻		pTE→sTM⁻		pTM→sTE⁻	
	$\theta = 0°$	$\theta = 45°$	$\theta = 0°$	$\theta = 45°$	$\theta = 0°$	$\theta = 45°$
GOS	8.81	135.2	131.7	129.8	132.2	130.1
GOI	9.25	140	138.7	136.3	138.6	136.1
GON	9.21	139.5	135.5	137.8	137.8	135.4

In particular, the GOS technology platform has been initially considered in simulations with threshold power levels intentionally limited to 450 mW. The results are plotted in Figs. 4(a)–4(c), corresponding to excitations: $p_{TE} \rightarrow s_{TE}^{-}$, $p_{TE} \rightarrow s_{TM}^{-}$, and $p_{TM} \rightarrow s_{TE}^{-}$, respectively. Furthermore, each state of polarization for the Stokes waves has been considered as acting independently, so that the fundamental features of the Raman laser emission can be derived very accurately. Indeed, an useful analytical closed-form formula has been demonstrated for the calculation of the threshold power, as in Eq. (8):

$$P_{th} = \left|S_{p,th}\right|^2 = \frac{L_{cavity}^2}{\kappa_p^2 v_{g,p}^2} \frac{\tau_s^{-1} A_{s\rho\sigma,p}^{SRS}}{v_{g,s} g_{bulk,Ge}^{SRS}} \left[\begin{array}{l} \left(\Delta\omega_p\right)^2 + \left(\dfrac{\tau_s^{-1} A_{s\rho\sigma,p}^{SRS}}{v_{g,s} g_{bulk,Ge}^{SRS}} \right)^2 \left(\dfrac{v_{g,p} n_2\big|_{\omega_p} \omega_p}{c_0 A_{p,p}^{Kerr}} \right)^2 + \\ +2\Delta\omega_p \left(\dfrac{\tau_s^{-1} A_{s\rho\sigma,p}^{SRS}}{v_{g,s} g_{bulk,Ge}^{SRS}} \right) \left(\dfrac{v_{g,p} n_2\big|_{\omega_p} \omega_p}{c_0 A_{p,p}^{Kerr}} \right) + \left(0.5\tau_p^{-1}\right)^2 \end{array} \right] \quad (8)$$

with $\Delta\omega_p = \omega_p - \omega_p^0 \cong -2\pi c_0 \left(\lambda_p - \lambda_p^0\right) / \lambda_p^2$, with λ_p and λ_p^0 the wavelength of the input pump and its closest cavity resonance, respectively.

The contour plots refer to a device architecture with a cavity length L_{cavity} = 1 cm, and a coupler gap g = 200 nm, exhibiting the effective SRS gains listed in Table 2 for θ = 45°. Moreover, the propagation loss coefficient (α_{loss}) evaluated by means of Eqs. (2)-(3), is assumed to be 1.5 dB/cm according to [2] and resulting in the unloaded cavity quality factor $Q_l = 2.15 \times 10^5$. Then, the pump wavelength is assumed to be perfectly matched to a racetrack resonator resonance (i.e., $\lambda_p = \lambda_p^0$), and the backward Stokes waves is considered as the expected excitation, according to the waveguide orientation aforementioned. The effects of mismatch between the Stokes wavelength and a racetrack resonance wavelength are discussed below. The investigation carried out leads to some important discussions: i) the threshold power generally decreases by decreasing κ_s^2 with κ_p^2 fixed at a specific value; ii) a specific value of the threshold power can be obtained with two quite distinct values of κ_p^2, by fixing a value of κ_s^2; iii) the Stokes power coupled out to the bus waveguide increases by increasing κ_s^2 for a given κ_p^2, thus imposing a trade-off between two conflicting requirements, low threshold power and high output Stokes power. Finally, it is worth noting that, since the values of the effective Raman gains associated to the excitations $p_{TE} \rightarrow s_{TE}^{-}$, $p_{TE} \rightarrow s_{TM}^{-}$, and $p_{TM} \rightarrow s_{TE}^{-}$ taken into account in Figs. 4(a)–4(c), respectively, are slightly similar, the resulting contour curves hold the same shape with analogous scales. A similar investigation is also proposed in Figs. 5(a)–5(c), where the Ge wire waveguide is assumed on the GON platform. As a result, the contour curves indicate that, for a fixed values of the pair (κ_s^2, κ_p^2), the GON technology platform can guarantee lower threshold powers than the GOS platform. As specificed previously, the considerations about the GON platform can be associated to the GOI material system without any approximation, since the simulation results are very similar.

#239685 Received 23 Apr 2015; revised 5 Jun 2015; accepted 8 Jun 2015; published 23 Jun 2015

The analysis of the threshold power as a function of pump and Stokes power coupling factors allows us to find important design guidelines for guided-wave directional couplers (DCs). Indeed, once the waveguide has been selected in order to maximize the effective Raman gain, any shape and architecture of the DCs can be practically designed and fabricated with the only requirement that the pair (κ_s^2 , κ_p^2) be chosen in order to achieve specific Raman laser performance (e.g., low threshold power). The generalized model implemented makes it possible to simulate and design any desired DC; for example a DC based upon S-bend waveguides has been employed in this investigation as sketched in Fig. 1(a), with L_{tr} = 220 μm and D = 30 μm, resulting in a bend radius longer than 350 μm in order to neglect any bending losses. Under this assumption, the threshold pump power as a function of the coupler length is plotted in Fig. 6(a). Furthermore, the excitations $p_{TE} \rightarrow s_{TE}^-$, $p_{TE} \rightarrow s_{TM}^-$, and $p_{TM} \rightarrow s_{TE}^-$, have been considered as a result of the previous discussions. Similarly, Fig. 6(b) shows a parallel analysis of the pump and Stokes coupling factors as a function of the coupler length. In this way, since a unique pair (κ_s^2 , κ_p^2) corresponds to a specific value of P_{th}, the same threshold power can be achieved independent of the particular DC architecture employed, provided that the same factors κ_s^2 , κ_p^2 are selected, thus resulting in a generalized design approach. By observing the curves in Fig. 6(a), a reasonable approach consists in selecting a proper DC configuration in order to minimize the threshold pump power required for the Raman lasing effect.

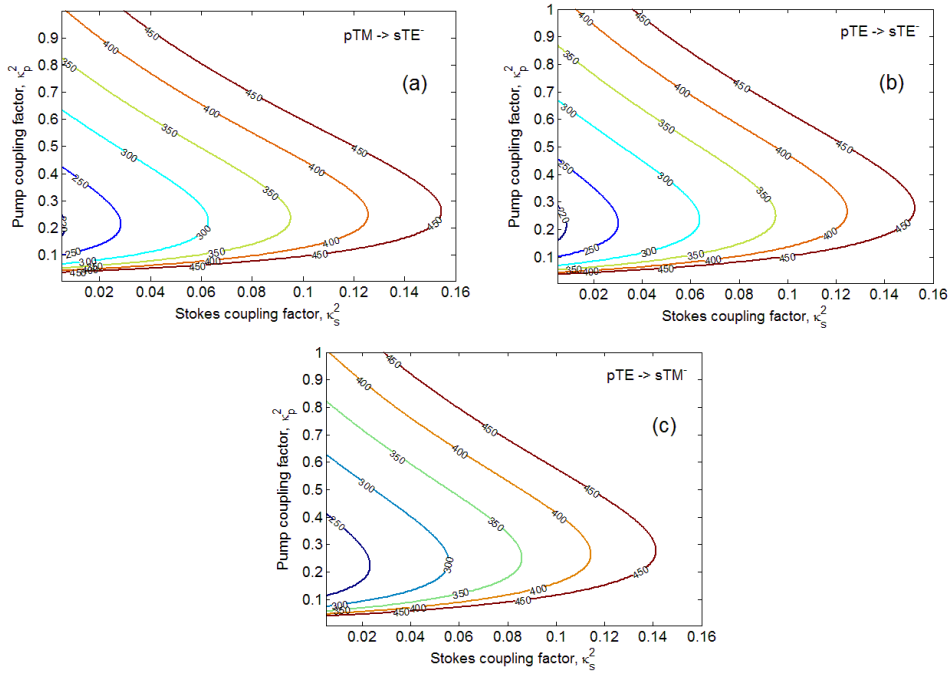

Fig. 4. Threshold power levels as a function of the pump and Stokes coupling factor; GOS platform: (a) $p_{TM} \rightarrow s_{TE}^-$; (b) $p_{TE} \rightarrow s_{TE}^-$; (c) $p_{TE} \rightarrow s_{TM}^-$.

#239685 Received 23 Apr 2015; revised 5 Jun 2015; accepted 8 Jun 2015; published 23 Jun 2015

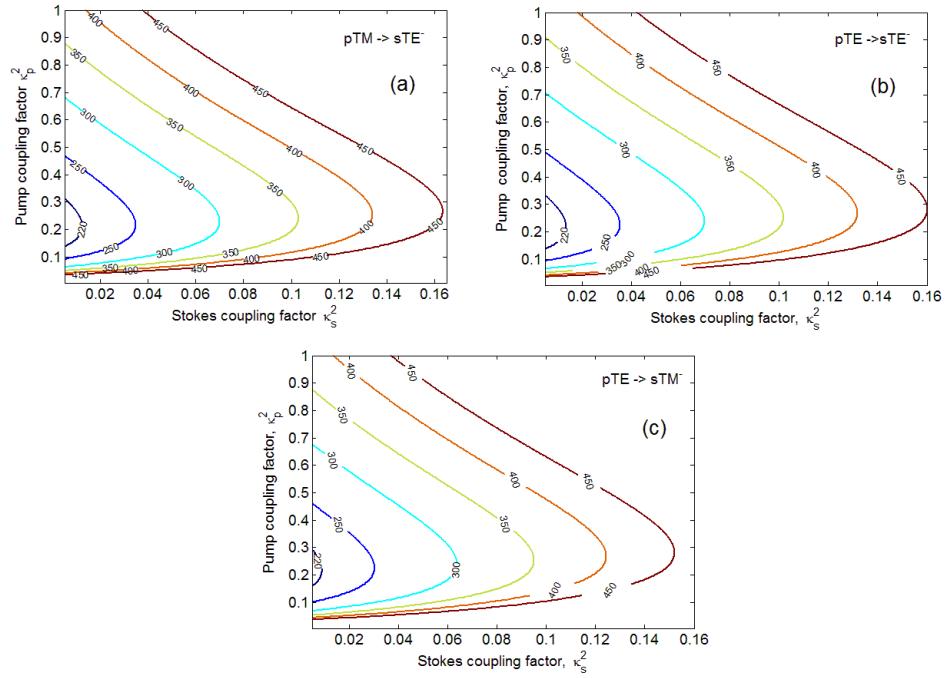

Fig. 5. Threshold power levels as a function of the pump and Stokes coupling factor; GON platform: (a) $p_{TM} \rightarrow s_{TE}^{-}$; (b) $p_{TE} \rightarrow s_{TE}^{-}$; (c) $p_{TE} \rightarrow s_{TM}^{-}$.

It is worth specifying that the results of the GOI platform are associated to the GON curves in Figs. 6(a) and 6(b), since they would be practically overlapped if plotted together. The analysis proposed in Fig. 6(a) imposes some considerations. Firstly, the GON and GOI platforms exhibit threshold pump powers lower than those achieved in GOS due to the higher effective Raman gains, as listed in Table 2.

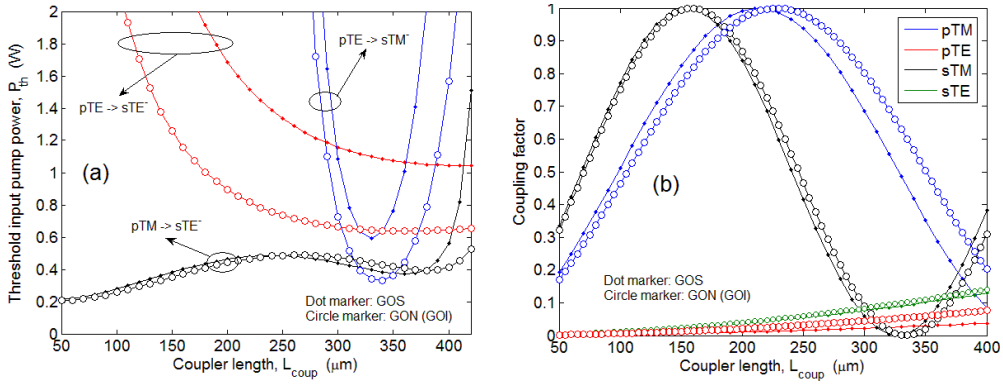

Fig. 6. (a) Threshold power as a function of the coupler length; (b) pump and Stokes coupling factors as a function of the coupler length.

Secondly, the excitation $p_{TM} \rightarrow s_{TE}^{-}$ presents a large range of L_{coup} (i.e., 50-310 μm for GON and 50-380 μm for GOS) in which threshold powers are less than 500 mW. Consequently, simulations plotted in Fig. 6(b) indicate that the corresponding coupling factors κ_s^2 vary in the ranges of [0.0038-0.088] and [0.0038-0.128] for GON and GOS platforms, respectively. Furthermore, a double solution for κ_p^2 can be chosen for a fixed κ_s^2, as previously discussed in

#239685 Received 23 Apr 2015; revised 5 Jun 2015; accepted 8 Jun 2015; published 23 Jun 2015

Figs. 4 and 5. A further consideration concerns the general trend of the excitations $p_{TE} \rightarrow s_{TE}^{-}$ and $p_{TE} \rightarrow s_{TM}^{-}$ which are characterized by very high threshold pump powers, corresponding to combinations of very low values of κ_p^2 and high values of κ_s^2 [Fig. 6(b)] and resulting in a reduced pump energy stored into the cavity and a large Stokes photon decay rate. In particular, a threshold power less than 500 mW for the excitation $p_{TE} \rightarrow s_{TM}^{-}$ in the case of GON and GOI platforms can be obtained by varying L_{coup} in the range [312-355] μm, but the excitation $p_{TM} \rightarrow s_{TE}^{-}$ is by far the best Raman excitation because of the very wide range of suitable values of L_{coup}, also suggesting large tolerances in the DC design.

The directionality and polarization state of the emitted Stokes signal inside the cavity are well-known at this stage of the analysis. Consequently, the influence of the mismatch between the input pump wavelength and the cavity resonances $\left(\lambda_p - \lambda_p^0\right)$ as well as between the Stokes wavelength and the cavity resonances $\left(\lambda_s - \lambda_s^0\right)$, is worth being investigated. To this purpose, the threshold pump power as a function of the pump wavelength mismatch and the cavity length is plotted in Fig. 7, assuming L_{coup} = 150 μm, and g = 200 nm. The three dimensional (3D) analysis reveals that the difference between the input pump and resonant wavelengths induces an increasing of threshold pump power, which is a detrimental effect for the Raman laser emission.

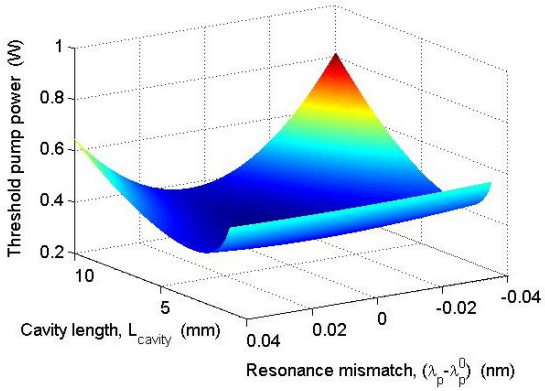

Fig. 7. Threshold pump power as a function of the wavelength mismatch and cavity length.

Furthermore, the influence of the mismatch $\left(\lambda_s - \lambda_s^0\right)$ affects the phase temporal evolution of the slowly varying field amplitude according to Eq. (9):

$$\frac{d\phi_s}{dt} = \left[\Delta\omega_s + \left(\frac{v_{g,s}\, n_2\big|_{\omega_s}\, \omega_s}{c_0 A_{s,s}^{Kerr}} \right) P_s + \left(\frac{2 v_{g,s}\, n_2\big|_{\omega_s}\, \omega_s}{c_0 A_{s\rho\sigma,p}^{Kerr}} \right) P_p \right] \tag{9}$$

with $\Delta\omega_s = \omega_s - \omega_s^0 \cong -2\pi c_0 \left(\lambda_s - \lambda_s^0\right) / \lambda_s^2$, and λ_s, and λ_s^0 the Stokes and cavity resonance wavelengths, respectively. The terms P_p and P_s indicate the steady-state values into the cavity for the pump and Stokes waves, respectively.

The detailed analysis of the Raman laser threshold is then completed by taking into account the simultaneous influence of the coupling length and the ratio W/H on P_{th}, as plotted in Figs. 8(a) and 8(b). In particular, the GOS platform as well as the excitations $p_{TM} \rightarrow s_{TE}^{-}$, and $p_{TE} \rightarrow s_{TM}^{-}$, L_{cavity} = 1 cm and g = 200 nm, have been considered in simulations while the maximum threshold power level is intentionally limited at 400 mW.

#239685 Received 23 Apr 2015; revised 5 Jun 2015; accepted 8 Jun 2015; published 23 Jun 2015

The contour curves in Fig. 8(a) clearly indicate that a decreasing of the threshold pump power can be obtained by reducing the ratio *W*/*H* because of higher effective Raman gains, and operating with DC lengths shorter than 100 μm. Moreover, the excitation $p_{TE} \rightarrow s^{-}_{TM}$ does not exhibit threshold powers less than 400 mW when *W*/*H* > 1. Furthermore, the comparative analysis presented in Figs. 8(a) and 8(b) suggests that the excitation $p_{TM} \rightarrow s^{-}_{TE}$ guarantees larger tolerances in the Raman laser design than excitation $p_{TE} \rightarrow s^{-}_{TM}$. The Stokes power emitted for the Raman racetrack laser is analyzed in the following as a function of DC fabrication tolerances. Indeed, Fig. 9 shows the output laser power ($P^{out}_{Stokes} = \kappa^2_s e^{-\alpha_s L_{bus}} P_s$) with L_{bus} = 150 μm μm of propagation from the coupler end) as a function of the DC gap and length, for $p_{TM} \rightarrow s^{-}_{TE}$ excitation, $P_{in} = |S_p|^2$ 500 mW and θ = 45°. The level curves represent the output Stokes power in mW. Figure 9 shows clearly the larger performance of GON platform with respect to the GOS technology.

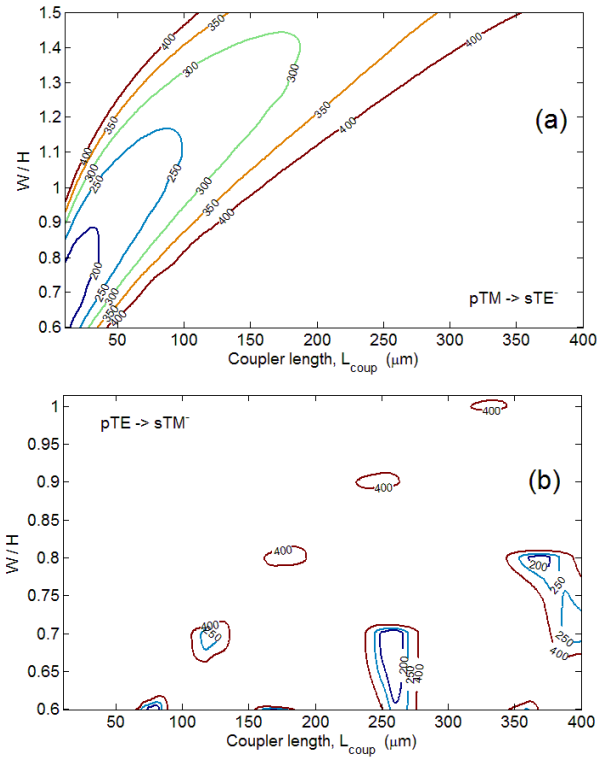

Fig. 8. Threshold power levels versus the W/H ratio and coupler length: (a) $p_{TM} \rightarrow s^{-}_{TE}$; (b) $p_{TE} \rightarrow s^{-}_{TM}$.

By assuming two well-determined conditions, i.e., i) CW regime, ii) unidirectional emission with only one polarization state, the Stokes power inside the cavity can be evaluated by a closed-form formula as:

$$P_s = \frac{-B + \sqrt{B^2 - 4AC}}{2A} \tag{10}$$

where the parameters *A*, *B* and *C* are defined as follows:

#239685 Received 23 Apr 2015; revised 5 Jun 2015; accepted 8 Jun 2015; published 23 Jun 2015

$$A = \frac{\tau_s^{-1} A_{s\rho\sigma,p}^{SRS}}{v_{g,s} g_{bulk,Ge}^{SRS}} \left[\left(\frac{2 v_{g,p} n_2\big|_{\omega_p} \omega_p}{c_0 A_{s\rho\sigma,p}^{Kerr}} \right)^2 + \left(\frac{0.5 v_{g,p} \lambda_s g_{bulk,Ge}^{SRS}}{\lambda_p A_{s\rho\sigma,p}^{SRS}} \right)^2 \right]$$

$$B = \frac{\tau_s^{-1} A_{s\rho\sigma,p}^{SRS}}{v_{g,s} g_{bulk,Ge}^{SRS}} \left[\begin{array}{l} 2\Delta\omega_p \left(\frac{2 v_{g,p} n_2\big|_{\omega_p} \omega_p}{c_0 A_{s\rho\sigma,p}^{Kerr}} \right) + \tau_p^{-1} \left(\frac{0.5 v_{g,p} \lambda_s g_{bulk,Ge}^{SRS}}{\lambda_p A_{s\rho\sigma,p}^{SRS}} \right) + \\ +2 \frac{\tau_s^{-1} A_{s\rho\sigma,p}^{SRS}}{v_{g,s} g_{bulk,Ge}^{SRS}} \left(\frac{2 v_{g,p} n_2\big|_{\omega_p} \omega_p}{c_0 A_{s\rho\sigma,p}^{Kerr}} \right) \left(\frac{v_{g,p} n_2\big|_{\omega_p} \omega_p}{c_0 A_{p,p}^{Kerr}} \right) \end{array} \right]$$

$$C = \frac{\tau_s^{-1} A_{s\rho\sigma,p}^{SRS}}{v_{g,s} g_{bulk,Ge}^{SRS}} \left[\begin{array}{l} \Delta\omega_p^2 + \left(\frac{\tau_s^{-1} A_{s\rho\sigma,p}^{SRS}}{v_{g,s} g_{bulk,Ge}^{SRS}} \right)^2 \left(\frac{v_{g,p} n_2\big|_{\omega_p} \omega_p}{c_0 A_{p,p}^{Kerr}} \right)^2 + \\ +2\Delta\omega_p \left(\frac{\tau_s^{-1} A_{s\rho\sigma,p}^{SRS}}{v_{g,s} g_{bulk,Ge}^{SRS}} \right) \left(\frac{v_{g,p} n_2\big|_{\omega_p} \omega_p}{c_0 A_{p,p}^{Kerr}} \right) + \left(0.5\tau_p^{-1} \right)^2 \end{array} \right] - \frac{\kappa_p^2 v_{g,p}^2}{L_{cavity}^2} \left| S_p \right|^2$$

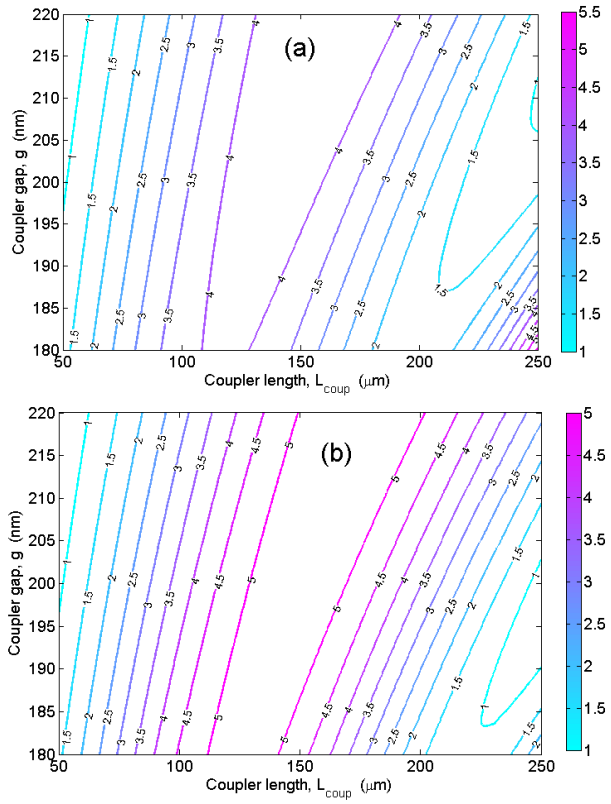

Fig. 9. Contour level curves of the output Stokes power as a function of coupler gap and length: a) GOS; b) GON.

The output Stokes power can be optimized by setting a proper value of the cavity length. In this context, Fig. 10(a) shows the output Stokes power as a function of the cavity length in case of GOS, GOI and GON technology platforms, assuming the $p_{TM} \rightarrow s_{TE}^{-}$ excitation, L_{coup} =

#239685 Received 23 Apr 2015; revised 5 Jun 2015; accepted 8 Jun 2015; published 23 Jun 2015

150 µm, g = 200 nm, θ = 45°, and a loaded quality factor Q_{tot} = 2.85 × 10^4. Simulations evidence the presence of an optimal condition represented by a curve peak. Indeed, by increasing more and more the cavity length, the SRS gain cannot compensate the propagation losses that the Stokes signal undergoes when traveling along multiple cavity roundtrips. Analogously, with decreasing more and more L_{cavity}, the Stokes signal excitation cannot occur when the pump signal propagates along a too short distance.

In the specific case study considered in this investigation (i.e., a Ge wire waveguide with $W = H$ = 2 µm), the optimal condition suitable for maximizing the Raman lasing is obtained for a cavity length L_{cavity} ≈2 mm, corresponding to a bend radius of about 130 µm. A possible limiting factor in the selection of the cavity length can be represented by the curvature radius, thus by the bending loss. To this purpose, the influence of the optical losses can be seen in Fig. 10(b), where the output Stokes power as a function of the input pump power and the overall loss coefficient (α_{loss}) are plotted. Simulations indicate that propagation losses of about 3 dB/cm require an input pump power larger than 800 mW in order to induce a lasing effect. Wavelength dependence of Ge-based Raman lasers has also been taken into account. To this purpose, the output Stokes power as a function of the pump signal wavelength is plotted in Fig. 11 for different values of the input pump power, in case of the GOS, GON, and GOI platforms. In particular, L_{coup} = 150 µm, g = 200 nm, θ = 45° and L_{cavity} = 1 cm, and a loaded quality factor Q_{tot} = 2.85 × 10^4 have been used in simulations.

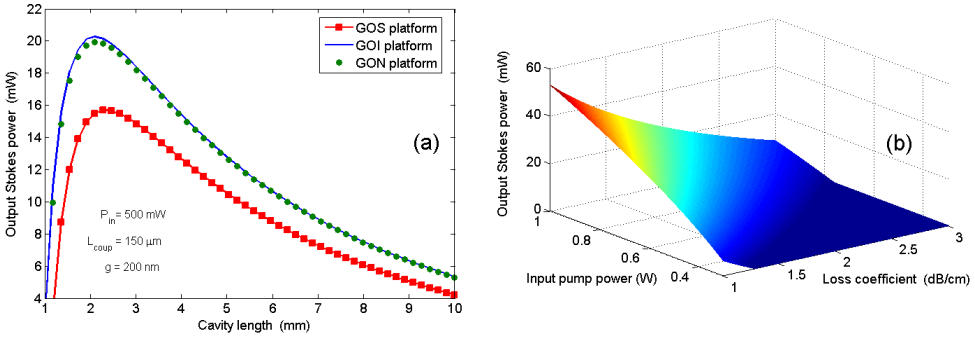

Fig. 10. (a) Output laser power versus the cavity length; (b) Output Stokes power versus the input pump power and loss coefficient.

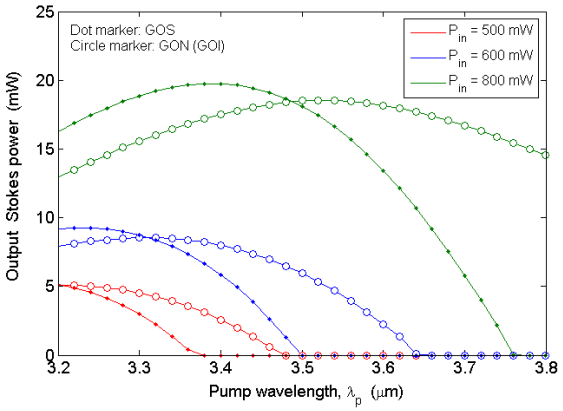

Fig. 11. Output Stokes power as a function of the pump wavelength for different values of the input pump power in the case of GOS, and GON (GOI) technology platforms.

It is worth noting that only the $p_{TM} \rightarrow s^{-}_{TE}$ excitation is shown in Fig. 11, since all the other excitations are rigorously under threshold for the wavelength range and the input pump

#239685 Received 23 Apr 2015; revised 5 Jun 2015; accepted 8 Jun 2015; published 23 Jun 2015

powers considered. Moreover, the plot indicates the presence of a specific threshold wavelength $\bar{\lambda}_p$, which causes the Raman laser inhibition and undergoes a blue shift by increasing the input pump power. This behavior is justified by the fact that the Stokes coupling factor monotonically increases in the wavelength range starting from 3.2 μm up to 3.8 μm, thus inducing an increasing of both threshold power (see Fig. 4) and Stokes power coupled to the bus waveguide. Furthermore, the value of $\bar{\lambda}_p$ in the case of GON and GOI platforms is higher compared to the GOS technology because of the larger effective Raman gains as also demonstrated in Table 2.

The analysis presented in this paper also includes the investigation of the laser time evolution by taking into account continuous wave (CW) and modulated input pump waves. To this purpose, the output laser power is shown in Fig. 12 by assuming the $p_{TM} \rightarrow s^{-}_{TE}$ excitation and GOS platform as well as the parameters L_{coup} = 150 μm, g = 200 nm, θ = 45° and L_{cavity} = 5 mm, P_{in} = 500 mW. Figures 12(a) and 12(b) represent the laser time responses when CW and square waves are used as input pumps, respectively. The plots have been obtained by solving numerically the set of five partial differential equations, according with the mathematical model presented in [21].

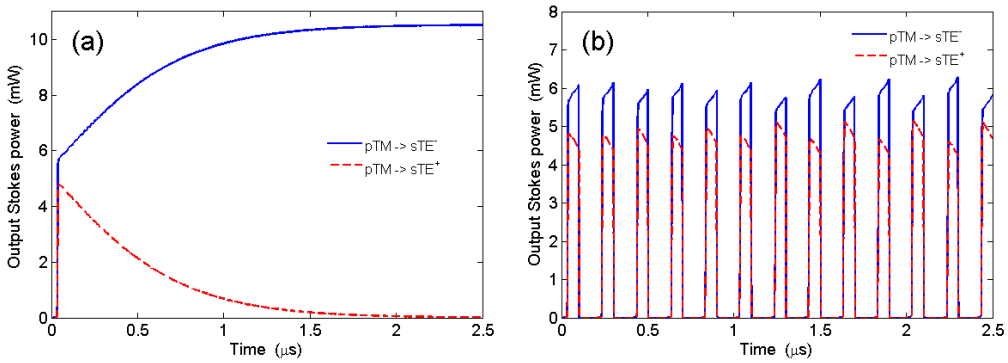

Fig. 12. (GOS platform) Time evolution of output laser power: (a) CW; (b) square wave modulation.

As a result, some considerations can be pointed out: i) the presence of both SPM and XPM effects produced by Kerr nonlinearity induces very weak oscillations in the laser time dynamics; ii) Fig. 12(a) clearly shows the laser unidirectionality induced by the amplification of the counter-propagating quasi-TE Stokes mode; iii) the solution system does not produce any amplification for s^{p}_{TM} waves; iv) Fig. 12(b) indicates that, for a pump wave modulated by a square wave with duty cycle of 50% and period of 200 ns, the bidirectional laser emission is induced, amplifying both co- and counter-propagating quasi-TE Stokes modes. Obviously, the bidirectionality can be obtained only if the period is shorter than the transient time needed to switch off the co-propagating Stokes wave, estimated in this specific case as 2 μs [Fig. 12(a)]; v) the power difference between the counter- and co-propagating Stokes waves increases by increasing the period of the input pump square wave.

4. Conclusions

In this paper a sophisticated full-vectorial mathematical model based on FEM has been implemented for investigating the performance of integrated Raman lasers based on GOS, GOI and GON technology platforms and operating in the MIR wavelength range of 3.2-3.8 μm, thus beyond the germanium TPA cut-off wavelength of 3.17 μm.

The influence of the annealing temperature in Ge deposition processes has been taken into account for the estimation of the Raman shift $\Omega_{Ge} - \Omega^{0}_{Ge}$ as a function of the temperature range

#239685 Received 23 Apr 2015; revised 5 Jun 2015; accepted 8 Jun 2015; published 23 Jun 2015

of 300-1000 °C. Numerical results show an overall variation $\Delta\left(\Omega_{Ge}-\Omega_{Ge}^{0}\right)$ of about 2 cm^{-1} in all cases of investigated technology platforms. Consequently, the effective Raman gains have been computed in Ge-based waveguides by taking into account both fixed and mixed TE and TM polarazations as well as the Ge crystallographic orientation. Then, fully-etched waveguides have been found to be more suitable than rib waveguides for achieving high Raman effective gain, since the effective SRS areas increase exponentially as a function of shallower etch depths. In particular, effective Raman gains vary as a function of the orientation angle θ similarly in all the technology platforms aforementioned. However, it is worth specifying that although Raman effective gains higher than 130 $(Wm)^{-1}$ can be achieved with θ ranging from 0° to 45° in the case of $p_{TE} \rightarrow s_{TM}^{-}$, and $p_{TM} \rightarrow s_{TE}^{-}$ excitations, similar high effective Raman gains can be achieved only with θ = 45° in the case of $p_{TE} \rightarrow s_{TE}^{-}$ excitation since $g_{s\rho}^{\sigma}$ as low as 9 $(Wm)^{-1}$ result with θ = 0°.

The analysis of the laser threshold power as a function of DC dimensions and power coupling factors for the pump and Stokes signal has revealed that $p_{TM} \rightarrow s_{TE}^{-}$ is by far the best Raman excitation because of the very wide range of suitable values of the DC length L_{coup} suitable for achieving threshold power lower than 600 mW with κ_s^2 less than 0.1 and κ_p^2 varying in the range 0-1, depending on the specific DC architecture to be designed. Moreover, the threshold power has also been computed as a function of the waveguide aspect ratio W/H, with the result that the excitation $p_{TM} \rightarrow s_{TE}^{-}$ exhibits threshold powers less than 400 mW when the ratio W/H is lower than 1.

The output Stokes power has been simulated as a function of racetrack overall length, input pump signal, overall proagation losses as well as input pump MIR wavelength varied in the range 3.2-3.8 μm. As a result, by assuming a fully-etched wire waveguide with $W = H = 2$ μm and an input pump power of 500 mW, an optimum cavity length of roughly 2 mm is found with the highest output power of 20 mW in the case of GOI and GON platforms, and of 16 mW in Raman lasers assumed in GOS technology. Furthermore, simulations indicate that propagation losses of about 3 dB/cm require an input pump power larger than 800 mW in order to induce a lasing effect. Consequently, low loss Ge waveguides as well as low bending losses are strongly suggested in order to achieve Raman lasing effect in Ge-based Raman lasers operating in the MIR. In addition, it is worth specifying that a rigorous design of the DCs should be carried out since the output Stokes power drops down as a function of longer input pump wavelengths because of the wavelength dependence of the pump and Stokes power coupling factors. Furthermore, the difference between the input pump and racetrack resonant wavelengths induces an increasing of the threshold pump power which is a detrimental effect for the Raman laser emission. On the contrary, the influence of the mismatch $\left(\lambda_s-\lambda_s^0\right)$ affects the phase temporal evolution of the slowly varying field amplitude. In conclusion, the simulation of the Raman laser in CW and pulse regime has revealed that the presence of both SPM and XPM effects produced by the Kerr nonlinearity induces very weak oscillations in the laser time dynamics.

In conclusion, regarding the Ge Raman laser, the choice of the lasing wavelength (essentially the choice of pump wavelength) determines which Ge waveguide platform is best for the laser. The two primary waveguide candidates are Ge-on-silicon-nitride (GON) and Ge on- bulk-Si (GOS). At a lasing wavelength < 7 μm, for example, the GON platform is probably best because it offers a higher index contrast between the substrate and the Ge core than does the silicon substrate. On the other hand, if lasing is desired at longer wavelengths in the 7 to 16 μm range, the situation changes and the GOS platform offers lower propagation loss, even though the silicon substrate does have moderate phonon-related losses in the 8 to 18 μm spectral range (around 0.9 to 9 cm^{-1}). Finally, the GOI platform is also a good choice

#239685 Received 23 Apr 2015; revised 5 Jun 2015; accepted 8 Jun 2015; published 23 Jun 2015

in the 3 to 4 μm spectral range, competitive there with GON. In summary, we can conclude that the GOS, GOI and GON technology platforms examined in this investigation are suitable for the design and fabrication of integrated Raman lasers operating in the MIR wavelength range, since they can generally exhibit larger Raman gains and lower losses than the SOI-based solutions. Moreover, the sophisticated and general approach used in this paper allows to extend the analysis presented here to any desired Ge-based waveguide structure and DC architectures, resulting in a very flexible design approach.

Acknowledgments

This work was supported in part by the Research Executive Agency under FP7 Project MERMIG (grant number 313037). R. A. Soref appreciates support of the Air Force Office of Scientific Research (FA9550-14-1-0196) and of the UK EPSRC Project MIGRATION (EP/L01162X/1).

#239685 Received 23 Apr 2015; revised 5 Jun 2015; accepted 8 Jun 2015; published 23 Jun 2015